ACS Photonics

Article

Cite This: ACS Photonics 2019, 6, 2841−2849

pubs.acs.org/journal/apchd5

Hot Electrons Modulation of Third-Harmonic Generation in Graphene

Giancarlo Soavi,[*,†,‡] Gang Wang,[†] Habib Rostami,[¶] Andrea Tomadin,[§] Osman Balci,[†] I. Paradisanos,[†] Eva A. A. Pogna,[∥] Giulio Cerullo,[∥] Elefterios Lidorikis,[⊥] Marco Polini,[§] and Andrea C. Ferrari[*,†]

[†]Cambridge Graphene Centre, University of Cambridge, Cambridge CB3 0FA, U.K.

[‡]Institut für Festkörperphysik, Friedrich-Schiller-Universität, Max-Wien-Platz 1, 07743 Jena, Germany

[¶]Nordic Institute for Theoretical Physics, Roslagstullsbacken 23, SE-106 91 Stockholm, Sweden

[§]Graphene Laboratories, Istituto Italiano di Tecnologia, Via Morego 30, I-16163 Genova, Italy

[∥]IFN-CNR, Dipartimento di Fisica, Politecnico di Milano, P.zza L. da Vinci 32, 20133 Milano, Italy

[⊥]Department of Materials Science and Engineering, University of Ioannina, Ioannina 45110, Greece

ABSTRACT: Hot electrons dominate the ultrafast (∼fs−ps) optical and electronic properties of metals and semiconductors, and they are exploited in a variety of applications including photovoltaics and photodetection. We perform power-dependent third-harmonic generation measurements on gated single-layer graphene and detect a significant deviation from the cubic power law expected for a third-harmonic generation process. We assign this to the presence of hot electrons. Our results indicate that the performance of nonlinear photonics devices based on graphene, such as optical modulators and frequency converters, can be affected by changes in the electronic temperature, which might occur due to an increase in absorbed optical power or Joule heating.

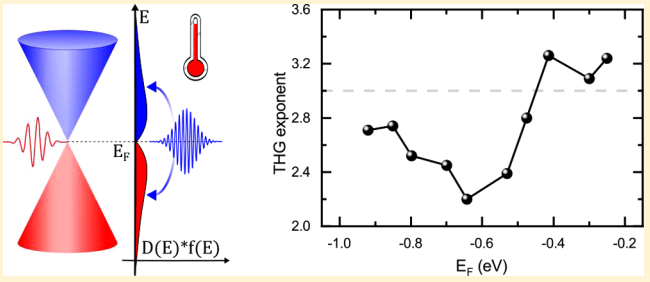

KEYWORDS: *graphene, hot electrons, third-harmonic generation, photonics, optoelectronics, nonlinear optics, ultrafast optics*

For a free electron gas at thermal equilibrium, the average occupation number at energy E is described by the Fermi−Dirac distribution $f(E)$:[1]

$$f(E) = \frac{1}{e^{(E-\mu)/k_B T_0} + 1} \quad (1)$$

where μ is the chemical potential and k_B is the Boltzmann constant. At zero temperature, μ equals the Fermi energy (E_F). At thermal equilibrium $T_e = T_l = T_0$, with T_e the electronic temperature, T_l the lattice temperature, and T_0 the ambient temperature. Photoexcitation of a sample with ultrashort (∼fs−ps) pulses creates a nonthermal regime, i.e., a condition where the electron population cannot be described by $f(E)$ and T_e, which rapidly evolves through electron−electron (e−e) scattering into a hot-carrier distribution, with $T_e > T_l$.[2−6] Electrons then transfer energy to the lattice through scattering with phonons (ph).[4−8] Equilibrium with the surrounding environment is then reached via ph−ph scattering until $T_e = T_l = T_0$.[4−13] The time scale of these scattering processes depends on the system under investigation and the excitation energy. Typical values for metals (e.g., Au, Ag, Cu, Ni[3,9−11]) and semiconductors (e.g., Si[7]) are ∼10 fs−1 ps for e−e scattering,[3] ∼1−100 ps for e−ph scattering,[7,8] and >100 ps for ph−ph scattering.[9−11] Hot electrons (HEs) can be exploited to enhance the efficiency of photocatalysis,[14] photovoltaic devices,[15,16] and photodetectors.[13] The efficiency of photovoltaic devices can be enhanced if HEs are collected before relaxation with ph,[16] when the absorbed light energy is transferred to the lattice instead of being converted into an electrical signal. Photodetectors based on the Seebeck effect[17] and Schottky junctions[18] both exploit HEs. These also play a key role in nonlinear effects, e.g., in second-harmonic generation (SHG)[19] and in third-harmonic generation (THG).[20] Following interaction with photons with energy $\hbar\omega_0$, where $\hbar$ is the reduced Planck constant and ω_0 is the photon angular frequency, new photons can be generated inside a nonlinear material at energies $2\hbar\omega_0$ for SHG[19] or $3\hbar\omega_0$ for THG.[20] In the scalar form, the SHG and THG optical electric field $\mathcal{E}_{m\omega_0}$ can be written as[21,22]

$$\mathcal{E}_{m\omega_0} = g\chi^{(m)}(\omega_0, E_F, T_e)\mathcal{E}^m_{\omega_0} \quad (2)$$

where $\mathcal{E}_{\omega_0}$ is the incident electric field, $m = 2$ for SHG and $m = 3$ for THG, g is a function of the material's refractive index (n) and ω_0, and $\chi^{(m)}$ is the material's nonlinear susceptibility. g and $\chi^{(m)}$ depend on material, angle, and polarization of the incident light and on m.[21−23] E.g., the THG field for a bulk sample for normal incidence and constant incident power is[21−23]

Received: June 30, 2019
Published: October 14, 2019

DOI: 10.1021/acsphotonics.9b00928
ACS Photonics 2019, 6, 2841−2849

$$\mathcal{E}_{3\omega_0} = \frac{1}{4}\frac{i3\omega_0}{2n_{3\omega_0}c} d\chi^{(3)}\mathcal{E}^3_{\omega_0} \quad (3)$$

where d is the material's thickness. The light intensity ($I_{m\omega_0}$ in units of W/m^2) is related to the optical electric field by $I_{m\omega_0} = n_{m\omega_0}\epsilon_0 c|\mathcal{E}_{m\omega_0}|^2/2$.[21−23] Equation 2 highlights two aspects of harmonic generation: (i) the SHG/THG electric field scales with the square/cube of $\mathcal{E}_{\omega_0}$ and, as a consequence, one would expect $I_{m\omega_0} \propto I^m_{\omega_0}$; (ii) the SHG/THG intensities depend on the linear (e.g., absorption) and nonlinear (through the nonlinear susceptibilities $\chi^{(2)}$ and $\chi^{(3)}$) properties of the material.[24,25] Both g and $\chi^{(m)}$ are functions of T_e and thus modify the power-law relation between $I_{m\omega_0}$ and $I^m_{\omega_0}$ because T_e depends, in turn, on the intensity I_{ω_0} of the illumination. The role of HEs in nonlinear optics was investigated for SHG in metals[10,25−29] and semiconductors[30,31] but, to the best of our knowledge, has not been considered thus far for THG in any material.

HEs also play a key role in the ultrafast (fs−ps)[5,6,32−34] nonlinear[35−37] properties of single-layer graphene (SLG). In SLG e−e scattering occurs within a few tens of fs after photoexcitation,[5] while e−ph scattering takes place on a ∼ps time scale.[5,34,38] HEs can be exploited for the development of SLG-based optoelectronic devices.[39−41] E.g., a SLG p−n junction can be used as a photothermal detector because, following optical excitation, the photothermoelectric (or Seebeck) effect will produce a voltage $V = (S_1 - S_2)\Delta T_e$, where $S_{1,2}$ (in V K^{-1}) are the thermoelectric powers (or Seebeck coefficients) and ΔT_e is the HEs temperature difference in the two SLG regions.[42,43] HEs in SLG can recombine radiatively to give broadband emission.[44−49] The time scale/mechanism of HEs relaxation have implications for the use of SLG in mode-locked lasers.[39,41,50] The interplay between HEs heating and cooling dynamics dominates linear[51] and nonlinear[52] THz response of SLG.

SLG can be used to fabricate broadband and gate-tunable optical frequency converters.[40,53−55] In these devices the high T_e (∼10^3 K) induced by optical excitation[5,46,53] can significantly modify (e.g., by reducing the THG efficiency, THGE, defined as the ratio between THG and incident intensities) the SLG nonlinear optical response.[53]

Here we demonstrate that for THG in SLG the cubic dependence[21,22] $I_{3\omega_0} \propto I^3_{\omega_0}$ fails when $T_e \gg T_l$ is taken into account. We show that, more generally, THG follows a power law $I_{3\omega_0} \propto I^x_{\omega_0}$, with the exponent x dependent on E_F. Our results are the first experimental evidence of the impact of HEs on a coherent third-order nonlinear optical process in any material.

A power law with exponent 3 was used since the first experimental demonstration of THG in 1962[20] to fit the data of experiments in all research areas, from fundamental science[20] to microscopy[56] and material characterization,[57] and any type of material including gases,[58] biological samples,[56] metals,[59] semiconductors,[57,60] hybrid nanostructures[61] and layered materials.[23,62−65] Here we change one of the paradigms of nonlinear optics and we show that the third-order nonlinear susceptibility of a medium can be controlled by the driving pulse through electron heating effects. We prove that THGE can either increase or decrease for increasing T_e depending on E_F, with values of the power-dependent THG exponent between 2 and 3.4. These findings have impact on the development of graphene photonic and optoelectronic devices, such as high-speed gate-tunable nonlinear optical switches and frequency converters.

We use chemical vapor deposition (CVD) SLG transferred on fused silica (FS) and gated by ionic liquid (IL), as sketched in Figure 1a. SLG is grown on Cu (99.8% pure, 25 μm thick),

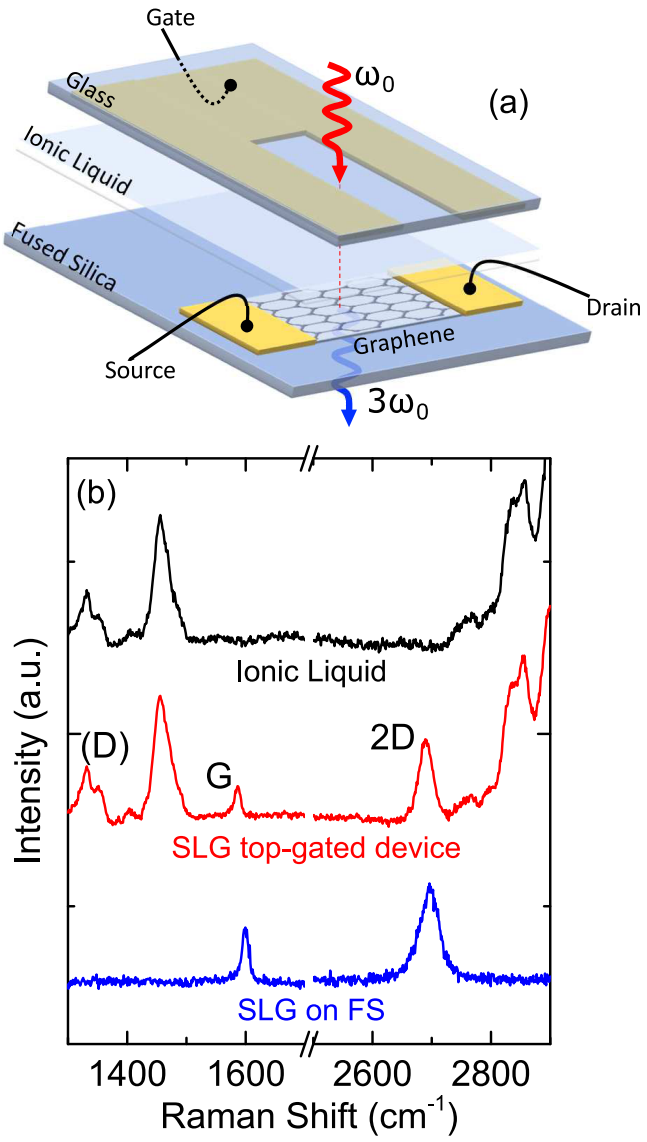

Figure 1. (a) Schematic of THG device. E_F tuning is obtained by IL top-gating. Measurements are performed in transmission. (b) 514 nm Raman spectra of SLG after transfer on FS (blue), SLG top-gated device (red), and IL (black).

as for ref 66. This is then transferred on FS by polymer-assisted Cu wet etching,[67] using poly(methyl methacrylate) (PMMA). SLG is characterized by Raman spectroscopy with a Renishaw inVia spectrometer. The 514 nm Raman spectrum of SLG after transfer is shown in Figure 1b. The 2D peak is a single Lorentzian with full width at half-maximum FWHM(2D) ∼ 36 cm^{-1}, a signature of SLG.[68] The position of the G peak, Pos(G), is ∼1599 cm^{-1}, with FWHM(G) ∼ 13 cm^{-1}. The 2D peak position is Pos(2D) ∼2696 cm^{-1}, while the 2D to G peak intensity and area ratios, I(2D)/I(G) and A(2D)/A(G), are ∼1.7 and ∼4.67, indicating a p-doping ∼250−300 meV.[69,70]

DOI: 10.1021/acsphotonics.9b00928
ACS Photonics 2019, 6, 2841−2849

The absence of the D peak shows that there are no significant defects. In order to gate the SLG, we fabricate source and drain contacts by evaporating 7 nm/70 nm Cr/Au. Cr is used to improve Au adhesion. We etch the SLG outside the channel using an oxygen plasma. As gate electrode we use 7 nm/70 nm Cr/Au on a 1 mm thick microscope slide. During evaporation, we cover part of the slide to have a transparent region ~1 cm^2 for optical measurements. We use 50 μm double-sided tape as a spacer between gate electrode and SLG. We then align SLG and the nonevaporated window on the gate electrode and place the IL, diethylmethyl(2-methoxyethyl)ammoniumbis(trifluoromethylsulfonyl)imide ($C_6H_{20}F_6N_2O_5S_2$), between SLG and gate electrode.

The 514 nm Raman spectra of IL and SLG at a gate voltage V_G = 0 V are shown in Figure 1b. For SLG, Pos(G) is ~1587 cm^{-1}, with FWHM(G) ~ 14 cm^{-1}. Pos(2D) ~ 2691 cm^{-1}, FWHM(2D) ~ 32 cm^{-1}, with I(2D)/I(G) and A(2D)/A(G) ~2.9 and ~5.9, respectively, indicating a p-doping ~200 meV.[69] Figure 2a,b plot the Raman and transmission spectra as a function of V_G from 0.4 to −1.6 V with steps of 0.1 V for a source−drain voltage V_{SD} = 0.2 V. From the spectra at different V_G we estimate E_F. This is done by monitoring the evolution of Pos(G) as a function of V_G, as shown in Figure 3.[69,70] The relation between E_F and V_G can also be derived from the transmission measurements. For each V_G, we measure both transmission, Figure 2b, and source−drain current, I_{SD}, Figure 4b (red circles). The transmission of the gated device never reaches 100%, defined as the transmission of the device without SLG. This nonsaturable residual absorption (α_{res}) of SLG originates from intraband electronic transitions, enabled by disorder.[71] From Figure 2b we get α_{res} ~ 0.2−0.4%, by taking the difference between the background (gray curve) and the SLG transmission at 0.8 eV for V_G = −1.4 V. The transition from intra- to interband absorption, at T_e = 0, occurs when the energy of the photons is $\hbar\omega = 2|E_F|$. For $T_e > 0$ K the absorption around $\hbar\omega = 2|E_F|$ broadens (Figures 2b, 4c) due to thermal broadening of the Fermi−Dirac distribution (eq 1). We thus estimate $\hbar\omega$ from the half-maximum of each transmission curve and calculate $E_F = \hbar\omega/2$, as in Figure 4a (red circles). This is in good agreement with the Raman analysis (blue circles in Figure 4a).

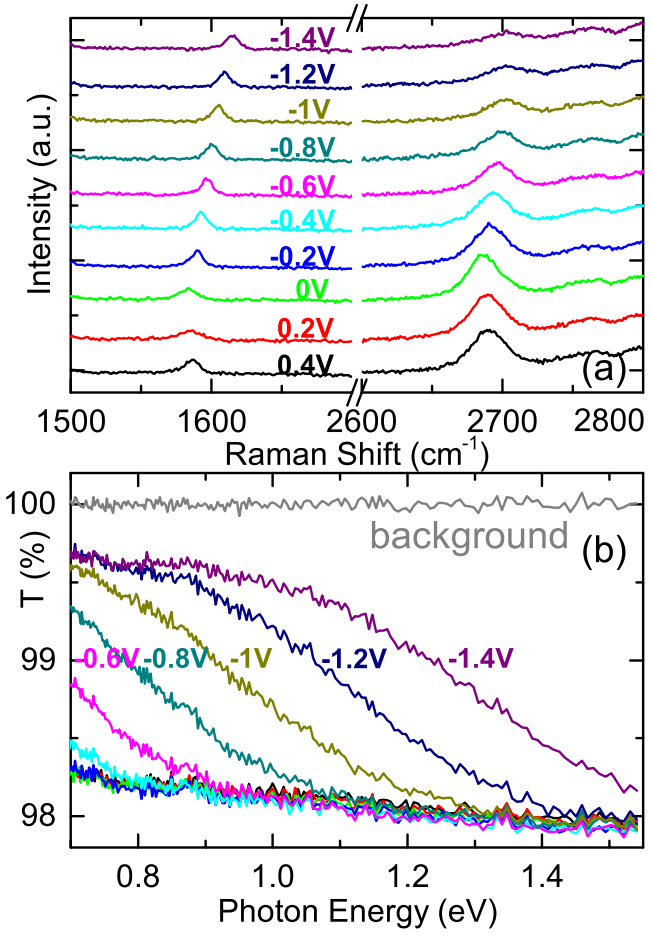

Figure 2. (a) Raman and (b) transmission spectra of an SLG top-gated device at different V_G. The background (100%) for the transmission spectra is defined as the transmission of the device without SLG.

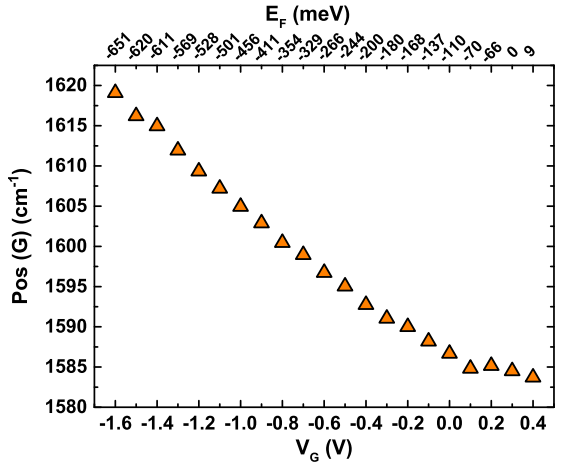

Figure 3. Pos(G) as a function of V_G from the Raman measurements in Figure 2a. E_F (top horizontal axis) is obtained as detailed in ref 69.

THG measurements are then performed at room temperature (RT). We excite the sample with the idler beam of an optical parametric oscillator (OPO, Coherent) at 0.69 eV (~1.8 μm) pumped by a mode-locked Ti:Sa laser (Coherent) with 150 fs pulse duration, 80 MHz repetition rate, and 4 W average power at 1.55 eV. The OPO idler is focused by a 40× reflective objective (Ag coating, numerical aperture NA = 0.5) to avoid chromatic aberrations. The THG signal is collimated by an 8 mm lens and delivered to a spectrometer (Horiba iHR550) equipped with a nitrogen-cooled Si charged-coupled device (CCD). The idler spot size is ~4.7 μm, the pulse duration is ~300 fs, and the polarization is linear. We use a Keithley 2612B dual-channel source measure unit both to apply V_G and V_{SD} and to read I_{SD}. V_G is tuned between −1.5 and +0.5 V, while V_{SD} is kept at 0.2 V. For THG measurements we tune V_G (10 points between −1.5 and +0.5 V) and scan the power (7 points between 1 and 4 mW). The incident excitation power is estimated at the sample position by measuring the power before and after the objective when the sample is removed. For each power (at a fixed V_G), we measure the THG signal by using 10s acquisition time and three accumulations. During THG experiments we also measure I_{SD}. By comparing the transconductance (I_{SD} as a function of V_G) during transmission, Figure 4b (red curve), and THG measurements, Figure 4b (black curve), we observe an increase in SLG doping. We thus estimate E_F based on I_{SD}, Figure 4a (black curve). SLG has a p-doping ~400 meV at V_G = 0 V

DOI: 10.1021/acsphotonics.9b00928
ACS Photonics 2019, 6, 2841−2849

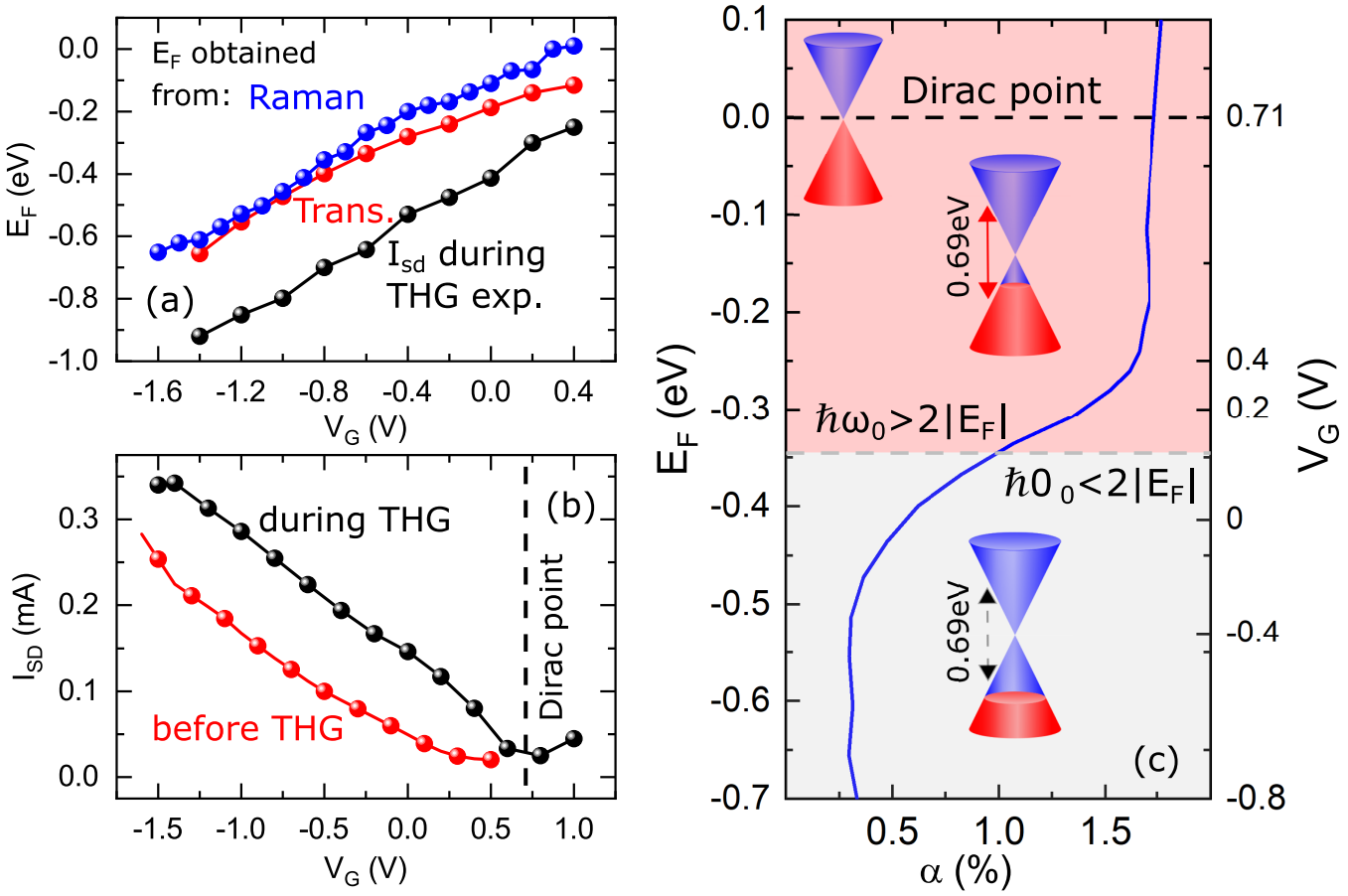

Figure 4. (a) E_F as a function of V_G obtained from the Raman analysis in Figure 3 (blue dots) and from the transmission measurements in Figure 2b (red dots). The black dots are E_F during THG experiments calculated from I_{SD}. (b) I_{SD} as a function of V_G before (red dots) and during (black dots) THG experiments. (c) Absorption at $\hbar\omega_0 = 0.69$ eV. The gray dotted line is at $E_F = \hbar\omega_0/2$. Absorption in the red region ($|E_F| < \hbar\omega_0/2$) is due to interband transitions, while in the gray region ($|E_F| > \hbar\omega_0/2$) interband transitions are forbidden (at $T_e = 0$ K) and absorption arises from intraband transitions.

(Figure 4a,c). From this we derive E_F between ∼−1 and +0.1 eV. This range covers both interband and intraband transitions for $\hbar\omega_0 = 0.69$ eV (Figure 4c), allowing us to perform a detailed analysis of the effect of E_F over the THG exponent. In order to estimate the emitted THG power, we take into consideration the losses of the system. The major ones are the absorption of the device without SLG (FS substrate and IL), the grating efficiency, and the CCD quantum efficiency. The transmission of the FS substrate is ∼93%, Figure 5. The IL transmission is frequency dependent, Figure 5 (red curve). We use the spectrometer specs[72] to estimate losses due to grating and CCD, and we account for the ∼7 CCD gain, i.e., the number of electrons for 1 count.[72]

The THG intensity $I_{3\omega_0}$ under normal incidence can be written as[53]

$$I_{3\omega_0} = f(\omega_0)\frac{I_{\omega_0}^3}{4\epsilon_0^4 c^4}|\sigma_{llll}^{(3)}(\omega_0, E_F, T_e)|^2 \quad (4)$$

where $\epsilon_0 \sim 8.85 \times 10^{-12}$ C(V m)$^{-1}$ and $c = 3 \times 10^8$ m/s are the vacuum permittivity and the speed of light; $f(\omega_0) = n_1^{-3}(\omega_0)n_2(3\omega_0)[n_1(3\omega_0) + n_2(3\omega_0)]^{-2}$ with $n_{i=1,2}(\omega)$ the IL ($i = 1$) and substrate ($i = 2$) refractive index. $\sigma_{llll}^{(3)}$ is the SLG third-order nonlinear optical conductivity tensor, calculated through a diagrammatic technique, with the light−matter interaction in the scalar potential gauge in order to capture all intraband, interband, and mixed transitions (see Methods for details).[36,53] According to the C_{6v} point group symmetry of SLG on a substrate, the relative angle between laser polarization and SLG lattice is not important for the third-order response.[53] Thus, we assume the incident polarization, $\hat{l}$, to lie along the zigzag direction of the lattice, $\hat{x}$, without loss of generality.[53] For IL we use[73] $n_1(\omega_0) \sim 1.44$ and for FS[73]

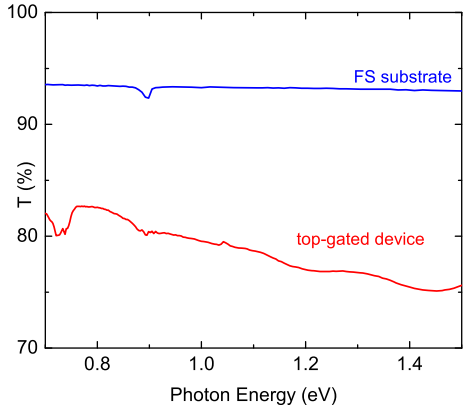

Figure 5. UV−vis transmission curves for substrate (FS) and device (IL and FS) without SLG.

DOI: 10.1021/acsphotonics.9b00928
ACS Photonics 2019, 6, 2841−2849

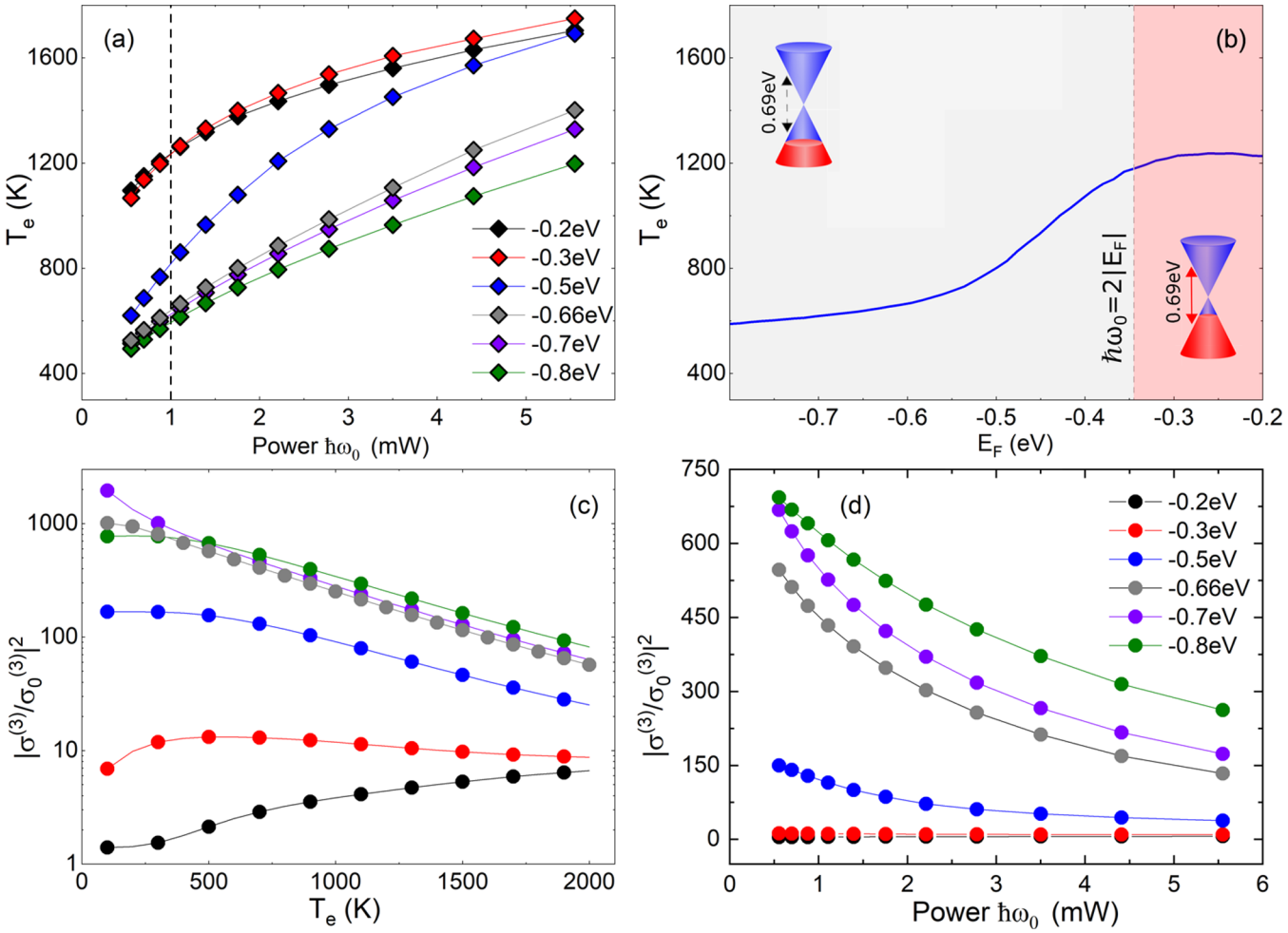

Figure 6. (a) T_e from eq 6 as a function of incident power for $\hbar\omega_0$ = 0.69 eV and different E_F. (b) T_e as a function of E_F from eq 6 for $\hbar\omega_0$ = 0.69 eV and 1 mW average power (black dotted line in panel a). The gray dotted line is at $\hbar\omega_0 = 2|E_F|$. (c) $|\sigma^{(3)}/\sigma_0^{(3)}|^2$ as a function of T_e for $\hbar\omega_0$ = 0.69 eV and different E_F in a single-chemical potential model. (d) $|\sigma^{(3)}/\sigma_0^{(3)}|^2$ as a function of incident power for $\hbar\omega_0$ = 0.69 eV and different E_F. The conversion from T_e to power is based on panel a.

$n_2(3\omega_0) \sim 1.42$. At first sight, eq 4 predicts a cubic dependence $I_{3\omega_0} \propto I_{\omega_0}^3$. However, $I_{3\omega_0}$ is modulated also by $\sigma_{llll}^{(3)}$, which is a function of ω_0, E_F, and T_e. ω_0 and E_F can be controlled by tuning the excitation energy and by applying V_G. T_e cannot be directly controlled by an external input, and its value is affected by the amount of energy transferred from light to the SLG electrons. T_e can be calculated from the Boltzmann equation, taking into account the role of intra- and interband e−e scattering and the population of the optical phonon modes.[6] An estimate can also be obtained with the following approach.[53] When a pulse of duration Δt and fluence $\mathcal{F}$ [J m^{-2}] photoexcites SLG, an average power per unit area $P/A = (\alpha + \alpha_{res})\mathcal{F}/\Delta t$ is absorbed by the electronic system, where α is the saturable SLG absorption, due to interband electronic transitions, which depends on the chemical potentials in conduction and valence bands (μ_c and μ_v) and T_e. The variation dU of the energy density in a time interval dt is dU = (P/A)dt. The corresponding T_e increase is dT_e = dU/c_v, where c_v is the electronic heat capacity of the photoexcited SLG. This is defined as[74] dU/dT_e (with U the energy density of the system) and depends on all parameters affecting U and T_e, including the SLG E_F and the absorbed power. Thus, in our model, we calculate c_v for each E_F and $\hbar\omega_0$. When the pulse is off, T_e relaxes to T_0 on a time scale τ. This reduces T_e by dT_e = $-(T_e/\tau)$dt in a time dt. Thus,[53]

$$\frac{dT_e}{dt} = \frac{\alpha + \alpha_{res}}{c_v}\frac{\mathcal{F}}{\Delta t} - \frac{T_e - T_0}{\tau} \quad (5)$$

If the pulse duration is (i) much longer than ∼20 fs, i.e., the time scale for the e distribution to relax to the Fermi−Dirac profile in both bands;[5,75] (ii) comparable to the time scale $\tau \sim$ 100−200 fs needed to heat the optical ph modes,[4,5,75] the electronic system reaches a steady state during the pulse, with T_e obtained from eq 5:

$$T_e = T_0 + \tau\frac{\alpha + \alpha_{res}}{c_v}\frac{\mathcal{F}}{\Delta t} \quad (6)$$

Figure 6a plots T_e from eq 6 for our experimental conditions: excitation power ∼ 0.5 mW to 5 mW, $E_F \sim -0.8$ to −0.2 eV, $\hbar\omega_0$ = 0.69 eV, T_0 = 300 K, τ = 100 fs, α_{res} = 0.4%, and Δt = 300 fs. A direct experimental measurement of T_e is not possible. We show here that, in power-dependent THG experiments, the indirect effect of T_e on the nonlinear optical properties of SLG can be observed. In fact, an increase of the excitation power induces an increase of T_e, thus modulating $\sigma^{(3)}$. The increase in T_e is also modulated by changes in E_F, as

DOI: 10.1021/acsphotonics.9b00928
ACS Photonics 2019, 6, 2841−2849

this affects α of SLG (Figure 2b). T_e rises steeply at $\hbar\omega = 2|E_F|$ due to a difference in absorption between interband and intraband transitions (Figure 6b).

Figure 6c shows the T_e dependence of $|\sigma^{(3)}/\sigma_0^{(3)}|^2$ in the 0–2000 K range and for different E_F, with[53] $\sigma_0^{(3)} = N_f e^4 \hbar v_F^2/[32\pi(1\text{ eV})^4]$. $\sigma_{IIII}^{(3)}$ converges to zero as $\sim 1/T_e$ for all values of E_F for increasing T_e (see Methods). $N_f = 4$ is the number of Fermion flavors, defined as the product between the spin (×2) and valley (×2) degrees of freedom in SLG,[36,53,76] and $v_F \sim 10^6$ m/s is the Fermi velocity; thus[53] $\sigma_0^{(3)} \sim 4.2 \times 10^{-24}$ A m^2/V^3. Figure 6d shows $|\sigma^{(3)}/\sigma_0^{(3)}|^2$ (same as Figure 6c) as a function of the incident power.

Figure 7a plots the experimental THG power dependence for $\hbar\omega_0 = 0.69$ eV. For the same values of incident power we do not detect any THG signal from FS/IL, i.e., outside the area covered by SLG. For a fixed incident power, the THG power increases as we go to more negative values of E_F. This E_F-dependent enhancement of the THG signal arises from logarithmic resonances in the imaginary part of the nonlinear conductivity of SLG due to resonant multiphoton transitions.[53,54] As seen in Figure 6b, this leads to a nonmonotonic dependence of the nonlinear conductivity on T_e for different E_F. We fit the experimental data relative to our THG power-dependent measurements (circles in Figure 7a) with the power law $y = ax^b$ (dotted lines in Figure 7a), where y is the $3\hbar\omega_0$ power, x is the incident power, and a and b are fitting parameters. Figure 7a shows that the power-law approximation gives excellent fits to the data, if we allow b to depend on E_F. Figure 7b plots b (i.e., the THG exponent) from this fit (black circles) as a function of E_F. The error bars in Figure 7a are defined as the standard deviation considering the average power stability of the fundamental beam (±0.7% over 30 min) and day-to-day alignment (±1.1%). We use the variance formula of the error propagation for a function $f = f(x, y, z)$:[77] $\sigma(f) = \sqrt{(\delta f/\delta x)\sigma_x^2 + (\delta f/\delta y)\sigma_y^2 + (\delta f/\delta z)\sigma_z^2}$, where σ is the standard deviation. For a power law $y = ax^b$, the standard deviation is $\sigma_y \sim |(yb\sigma_x)/x|$. In our case $y = P_{3\hbar\omega_0}$ and $y = P_{\hbar\omega_0}$. b is obtained from fitting the experimental data and is $2.2 < b < 3.4$ depending on E_F. The error bars in Figure 7b reproduce the standard deviation of the power-law fitting $y = ax^b$. The error in our measurements does not affect the evidence of a significant deviation of the THG power law from a cubic function. The dotted lines in Figure 7b are the theoretical b (THG exponent) calculated as follows: (i) T_e and corresponding μ_C and μ_v as a function of incident power are derived from eq 6, for $\hbar\omega_0 = 0.69$ eV and different E_F; (ii) we use these to calculate $\sigma^{(3)}$ as a function of incident power. To this end, we first calculate the $T_e = 0$ expression of the third-order nonlinear conductivity[36] and then utilize the response function in ref 6 to express the conductivity at finite T_e as a weighted integral over E_F of the SLG conductivity at $T_e = 0$ (see Methods for details); (iii) we substitute the calculated $\sigma^{(3)}$ into eq 4 to obtain the theoretical THG intensity; (iv) we fit the THG intensity with $y = ax^b$. For the estimate of T_e we use $\alpha_{res} = 0.2\%$ and 0.4%, as derived from Figure 2b. We find that the THG exponent varies between ∼2 and 3.4, with a nonmonotonic dependence on E_F and a minimum at $E_F \sim 0.6$ eV for $\hbar\omega_0 = 0.69$ eV. The dominant parameter that controls the deviation of the THG exponent from its expected value of 3 is T_e. The THG intensity scales as $I_{3\omega_0} \sim I_{\omega_0}^3 |\sigma_{IIII}^{(3)}(\omega_0, E_F, T_e)|^2$ (eq 4), and $\sigma_{IIII}^{(3)}$ depends on the input power because of its dependence on T_e: $|\sigma_{IIII}^{(3)}(\omega_0, E_F, T_e)|^2 \sim I_{\omega_0}^{\nu}$. Therefore, we have $I_{3\omega_0} \sim I_{\omega_0}^{3+\nu}$. T_e increases monotonically with incident power, and its variation depends on E_F (Figure 6a). Instead, $\sigma_{IIII}^{(3)}$ can either increase or decrease with incident power, depending on E_F (Figure 6d). $|\sigma_{IIII}^{(3)}(\omega_0, E_F, T_e)|^2$ is almost independent of input power, when $E_F \sim -0.3$ eV. Thus, the THG exponent is ∼3 in this case. When $E_F \sim -0.7$ eV, its variation is stronger and it has negative slope, leading to a THG exponent <3. The nonmonotonic evolution of the THG exponent and the presence of a minimum reflect the E_F and T_e dependence of $|\sigma_{IIII}^{(3)}(\omega_0, E_F, T_e)|^2$.

To the best of our knowledge, this noncubic behavior of the THG signal was not reported before in SLG or any other material. Most experiments on SLG and layered materials incorrectly took the observation of a cubic power law as a proof of third-order nonlinear effects.[23,62−65] In SLG, this cubic dependence was also used to calculate $\chi^{(3)}$.[23,63,64] This approach has two limitations: (1) the nonlinear susceptibilities are well defined only in three-dimensional materials, since they involve a polarization per unit volume,[53] and $\chi^{(3)}$ should not be

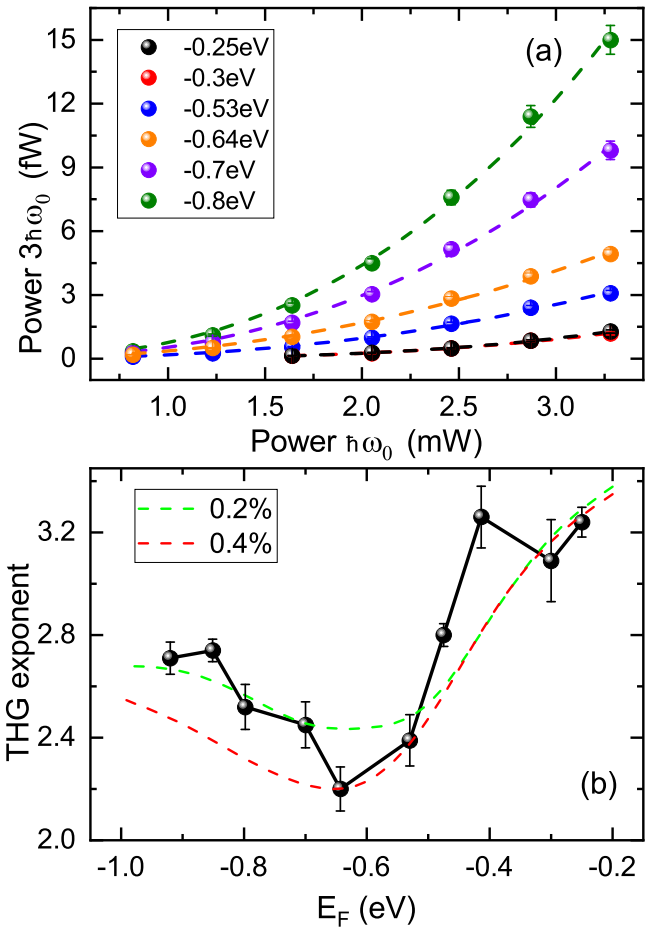

Figure 7. (a) $3\hbar\omega_0$ power as a function of incident power for different E_F. The dotted lines are obtained from the power law $y = ax^b$, with a and b fitting parameters. The error bars are defined considering the average power stability of the fundamental beam and day-to-day alignment. (b) THG exponent from fitting ($y = ax^b$) the power-dependent THG (black points) and from theory (dotted lines) for different α_{res} and $\hbar\omega_0 = 0.69$ eV. The error bars are the standard deviation of the power-law fitting function $y = ax^b$.

DOI: 10.1021/acsphotonics.9b00928
ACS Photonics 2019, 6, 2841−2849

used for SLG; (2) a power-law fit of THG in SLG must take into account E_F and T_e under the specific experimental conditions. Thus, $\chi^{(3)}$ must be calculated as a function of both E_F and T_e.

In summary, hot electrons affect the third-order nonlinear optical response of single-layer graphene and alter the cubic dependence of the third-harmonic generation signal and its efficiency. Upon ultrafast (~100 fs) excitation, T_e in single-layer graphene can be as high as 10^3 K also when $E_F > 2\hbar\omega_0$, due to thermal broadening of the Fermi−Dirac distribution and residual absorption. There is a fundamental difference between the THz nonlinear response in ref 52 and our experiments, regarding both the physics of the observed nonlinearities and the HEs role. The THz nonlinear signal of ref 52 arises from the deposition of energy into the electronic population and the consequent mismatch between the processes of HE heating and cooling with respect to the ~ps period of the THz electric field. This is, by definition, incoherent and nonparametric. In our work, HEs are a perturbation to a fully coherent and parametric THG process. In this context, changes in T_e can modify the third-harmonic generation efficiency, thus the performances of nonlinear photonic and optoelectronic devices, such as optical switches and frequency converters.

METHODS

$\sigma^{(3)}_{IIII}$ modeling. $\sigma^{(3)}_{IIII}$ is calculated using a diagrammatic technique, with the light−matter interaction in the scalar potential gauge in order to capture all intraband, interband, and mixed transitions.[35,36] We denote by $\Pi^{(3)}_l$ the response function. $\hat{n}$ and $\hat{j}_l$ are the density and paramagnetic current operators. Then, $\sigma^{(3)}_{IIII} = (ie)^3 \lim_{\vec{q}\to 0} \partial^3 \Pi^{(3)}_l / \partial q_l^3$, where $e > 0$ is the fundamental charge.[36] The Dirac Hamiltonian of low-energy carriers in SLG is $\mathcal{H}_k = \hbar v_F \vec{k}\cdot\vec{\sigma}$ where $\vec{\sigma} = (\pm\sigma_x, \sigma_y)$ are the Pauli matrices in the sublattice basis. ± represents the two valleys in the SLG Brillouin zone. We get $\sigma^{(3)}_{xxxx}(\omega, E_F, 0) = i\sigma_0^{(3)}\bar{\sigma}^{(3)}_{xxxx}(\omega, E_F, 0)$ at $T_e = 0$, with[35,36]

$$\bar{\sigma}^{(3)}_{xxxx}(\omega, E_F, 0) = \frac{17G(2|E_F|, \hbar\omega_+) - 64G(2|E_F|, 2\hbar\omega_+)|}{24(\hbar\omega_+)^4} + \frac{45G(2|E_F|, 3\hbar\omega_+)}{24(\hbar\omega_+)^4} \quad (7)$$

where $G(x, y) = \ln|(x + y)/(x - y)|$, $\sigma_0^{(3)} = N_f e^4 \hbar v_F^2/[32\pi (\mathrm{eV})^4]$ with $N_f = 4$, and $\hbar\omega_+ \equiv \hbar\omega + i0^+$ is in eV units. At finite T_e, $\sigma^{(3)}_{IIII}$ is evaluated as[78]

$$\sigma^{(3)}_{xxxx}(\omega, E_F, T_e) = \frac{1}{4k_B T_e} \int_{-\infty}^{\infty} dE \frac{\sigma^{(3)}_{xxxx}(\omega, E, 0)}{\cosh^2\left(\frac{E-\mu}{2k_B T_e}\right)} \quad (8)$$

THG Power Dependence. A THG power-dependent graph in log−log scale can show the deviation of the THG exponent b (i.e., the slope in log−log scale) from the expected value of 3. Figure 8 plots the THG power-dependent experiments (same as Figure 7a) in a log−log scale together with numerical examples of cubic THG dependence (gray lines). This shows that the power dependence is almost cubic for $E_F \sim -0.2$ and -0.3 eV, while there is a deviation from a slope of 3 for higher E_F.

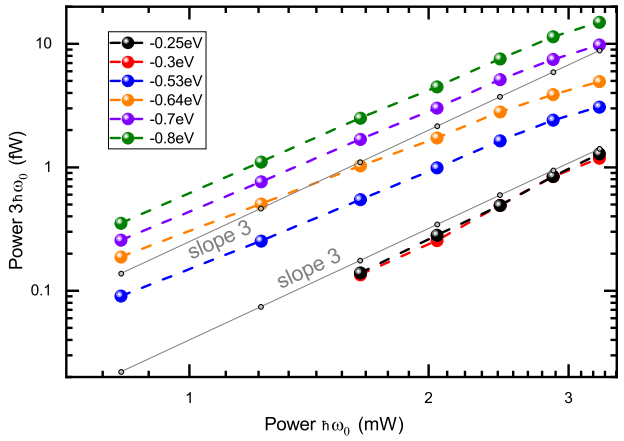

Figure 8. THG power as a function of incident power on a log−log scale. The gray lines are numerical examples of curves with slope 3 (cubic THG exponent b) and different prefactors a.

AUTHOR INFORMATION

Corresponding Authors

*E-mail: giancarlo.soavi@uni-jena.de.
*E-mail: acf26@eng.cam.ac.uk.

ORCID

Eva A. A. Pogna: 0000-0003-4779-3549
Giulio Cerullo: 0000-0002-9534-2702
Elefterios Lidorikis: 0000-0002-9552-9366
Andrea C. Ferrari: 0000-0003-0907-9993

Notes

The authors declare no competing financial interest.

ACKNOWLEDGMENTS

We acknowledge funding from EU Graphene Flagship, ERC Grants Hetero2D, GSYNCOR, EPSRC Grants EP/K01711X/1, EP/K017144/1, EP/N010345/1, EP/L016087/1, and the Swedish Research Council (VR 2018-04252).

REFERENCES

(1) Kittel, C. *Introduction to Solid State Physics*; Wiley: New York, USA, 1996.
(2) Fann, W. S.; Storz, R.; Tom, H. K.; Bokor, J. Direct measurement of nonequilibrium electron-energy distributions in subpicosecond laser-heated gold films. *Phys. Rev. Lett.* **1992**, *68*, 2834−2837.
(3) Della Valle, G.; Conforti, M.; Longhi, S.; Cerullo, G.; Brida, D. Real-time optical mapping of the dynamics of nonthermal electrons in thin gold films. *Phys. Rev. B: Condens. Matter Mater. Phys.* **2012**, *86*, 155139−6.
(4) Lazzeri, M.; Piscanec, S.; Mauri, F.; Ferrari, A. C.; Robertson, J. Electron Transport and Hot Phonons in Carbon Nanotubes. *Phys. Rev. Lett.* **2005**, *95*, 236802−4.
(5) Brida, D.; Tomadin, A.; Manzoni, C.; Kim, Y. J.; Lombardo, A.; Milana, S.; Nair, R. R.; Novoselov, K. S.; Ferrari, A. C.; Cerullo, G.; Polini, M. Ultrafast collinear scattering and carrier multiplication in graphene. *Nat. Commun.* **2013**, *4*, 1987.
(6) Tomadin, A.; Brida, D.; Cerullo, G.; Ferrari, A. C.; Polini, M. Nonequilibrium dynamics of photoexcited electrons in graphene: Collinear scattering, Auger processes, and the impact of screening. *Phys. Rev. B: Condens. Matter Mater. Phys.* **2013**, *88*, 035430−18.
(7) Shank, C. V.; Yen, R.; Hirlimann, C. Time-Resolved Reflectivity Measurements of Femtosecond-Optical-Pulse-Induced Phase Transitions in Silicon. *Phys. Rev. Lett.* **1983**, *50*, 454−457.

DOI: 10.1021/acsphotonics.9b00928
ACS Photonics 2019, 6, 2841−2849

(8) Schoenlein, R. W.; Lin, W. Z.; Fujimoto, J. G.; Eesley, G. L. Femtosecond studies of nonequilibrium electronic processes in metals. *Phys. Rev. Lett.* **1987**, *58*, 1680−1683.
(9) Vallée, F. Ultrafast spectroscopy of metals. *C. R. Acad. Sci., Ser. IV: Phys., Astrophys.* **2001**, *2*, 1469−1482.
(10) Hohlfeld, J.; Wellershoff, S.-S.; Güdde, J.; Conrad, U.; Jähnke, V.; Matthias, E. Electron and lattice dynamics following optical excitation of metals. *Chem. Phys.* **2000**, *251*, 237−258.
(11) Shah, J. *Ultrafast Spectroscopy of Semiconductors and Semiconductor Nanostructures*; Springer Science: New York, USA, 2013.
(12) Soavi, G.; Scotognella, F.; Lanzani, G.; Cerullo, G. Ultrafast Photophysics of SingleâĂŘWalled Carbon Nanotubes. *Adv. Opt. Mater.* **2016**, *4*, 1670−1688.
(13) Li, W.; Valentine, J. G. Harvesting the loss: surface plasmon-based hot electron photodetection. *Nanophotonics* **2017**, *6*, 177−191.
(14) Mukherjee, S.; Libisch, F.; Large, N.; Neumann, O.; Brown, L. V.; Cheng, J.; Lassiter, J. B.; Carter, E. A.; Nordlander, P.; Halas, N. J. Hot electrons do the impossible: plasmon-induced dissociation of H2 on Au. *Nano Lett.* **2013**, *13*, 240−247.
(15) Ross, R. T.; Nozik, A. J. Efficiency of hotâĂŘcarrier solar energy converters. *J. Appl. Phys.* **1982**, *53*, 3813−3818.
(16) Tisdale, W. A.; Williams, K. J.; Timp, B. A.; Norris, D. J.; Aydil, E. S.; Zhu, X. Y. Hot-Electron Transfer from Semiconductor Nanocrystals. *Science* **2010**, *328*, 1543−1547.
(17) Stiens, J.; Shkerdin, G.; Kotov, V.; Vandermeiren, W.; Tandt, C. D.; Borghs, G.; Vounckx, R. Seebeck infrared photodetectors: an ultra wide dynamic range of design possibilities. *Proc. SPIE* **2006**, *6189*, 61890Y.
(18) Shepherd, F. D.; Yang, A. C.; Taylor, R. W. A 1 to 2 μm silicon avalanche photodiode. *Proc. IEEE* **1970**, *58*, 1160−1162.
(19) Franken, P. A.; Hill, A. E.; Peters, C. W.; Weinreich, G. Generation of Optical Harmonics. *Phys. Rev. Lett.* **1961**, *7*, 118−119.
(20) Terhune, R. W.; Maker, P. D.; Savage, C. M. Optical Harmonic Generation in Calcite. *Phys. Rev. Lett.* **1962**, *8*, 404−406.
(21) Shen, Y. R. *The Principles of Nonlinear Optics*; Wiley: New York, USA, 1984.
(22) Boyd, R. W. *Nonlinear Optics*; Academic Press: New York, USA, 2003.
(23) Kumar, N.; Kumar, J.; Gerstenkorn, C.; Wang, R.; Chiu, H.-Y.; Smirl, A. L.; Zhao H, H. Third harmonic generation in graphene and few-layer graphite films. *Phys. Rev. B: Condens. Matter Mater. Phys.* **2013**, *87*, No. 121406R.
(24) Burns, W. K.; Bloembergen, N. Third-Harmonic Generation in Absorbing Media of Cubic or Isotropic Symmetry. *Phys. Rev. B* **1971**, *4*, 3437−3450.
(25) Hohlfeld, J.; Grosenick, D.; Conrad, U.; Matthias, E. Femtosecond time-resolved reflection second-harmonic generation on polycrystalline copper. *Appl. Phys. A: Mater. Sci. Process.* **1995**, *60*, 137−142.
(26) Guo, C.; Rodriguez, G.; Taylor, A. J. Ultrafast Dynamics of Electron Thermalization in Gold. *Phys. Rev. Lett.* **2001**, *86*, 1638−1641.
(27) Hohlfeld, J.; Conrad, U.; Matthias, E. Does femtosecond time-resolved second-harmonic generation probe electron temperatures at surfaces? *Appl. Phys. B: Lasers Opt.* **1996**, *63*, 541−544.
(28) Moore, K. L.; Donnelly, T. D. Probing nonequilibrium electron distributions in gold by use of second-harmonic generation. *Opt. Lett.* **1999**, *24*, 990−992.
(29) Papadogiannis, N.; Moustaizis, S. Nonlinear enhancement of the efficiency of the second harmonic radiation produced by ultrashort laser pulses on a gold surface. *Opt. Commun.* **1997**, *137*, 174−180.
(30) Tom, H. W. K.; Aumiller, G. D.; Brito-Cruz, C. H. Time-resolved study of laser-induced disorder of Si surfaces. *Phys. Rev. Lett.* **1988**, *60*, 1438−1441.
(31) Saeta, P.; Wang, J. K.; Siegal, Y.; Bloembergen, N.; Mazur, E. Ultrafast electronic disordering during femtosecond laser melting of GaAs. *Phys. Rev. Lett.* **1991**, *67*, 1023−1026.
(32) Bistritzer, R.; MacDonald, A. H. Electronic Cooling in Graphene. *Phys. Rev. Lett.* **2009**, *102*, 206410−4.
(33) Betz, A. C.; Vialla, F.; Brunel, D.; Voisin, C.; Picher, M.; Cavanna, A.; Madouri, A.; Féve, G.; Berroir, J. M.; Placais, B.; Pallecchi, E. Hot Electron Cooling by Acoustic Phonons in Graphene. *Phys. Rev. Lett.* **2012**, *109*, 056805−5.
(34) Tielrooij, K. J.; Song, J.; Jensen, S. A.; Centeno, A.; Pesquera, A.; Elorza, A. Z.; Bonn, M.; Levitov, L.; Koppens, F. Photoexcitation cascade and multiple hot-carrier generation in graphene. *Nat. Phys.* **2013**, *9*, 248−252.
(35) Mikhailov, S. A. Quantum theory of the third-order nonlinear electrodynamic effects of graphene. *Phys. Rev. B: Condens. Matter Mater. Phys.* **2016**, *93*, 085403−29.
(36) Rostami, H.; Polini, M. Theory of third-harmonic generation in graphene: A diagrammatic approach. *Phys. Rev. B: Condens. Matter Mater. Phys.* **2016**, *93*, 161411−5.
(37) Cheng, J. L.; Vermeulen, N.; Sipe, J. E. Third order optical nonlinearity of graphene. *New J. Phys.* **2014**, *16*, 053014−16.
(38) Lazzeri, M.; Piscanec, S.; Mauri, F.; Ferrari, A. C.; Robertson, J. Phonon linewidths and electron-phonon coupling in graphite and nanotubes. *Phys. Rev. B: Condens. Matter Mater. Phys.* **2006**, *73*, 155426−6.
(39) Bonaccorso, F.; Sun, Z.; Hasan, T.; Ferrari, A. C. Graphene photonics and optoelectronics. *Nat. Photonics* **2010**, *4*, 611−622.
(40) Romagnoli, M.; Sorianello, V.; Midrio, M.; Koppens, F. H. L.; Huyghebaert, C.; Neumaier, D.; Galli, P.; Templ, W.; D'Errico, A.; Ferrari, A. C. Graphene-based integrated photonics for next-generation datacom and telecom. *Nature Rev. Mater.* **2018**, *3*, 392−414.
(41) Ferrari, A. C.; Bonaccorso, F.; Fal'ko, V.; Novoselov, K. S.; Roche, S.; Boggild, P.; Borini, S.; Koppens, F. H. L.; Palermo, V.; Pugno, N.; et al. Science and technology roadmap for graphene, related two-dimensional crystals, and hybrid systems. *Nanoscale* **2015**, *7*, 4598−4810.
(42) Gabor, N. M.; Song, J. C. W.; Ma, Q.; Nair, N. L.; Taychatanapat, T.; Watanabe, K.; Taniguchi, T.; Levitov, L. S.; Jarillo-Herrero, P. Hot CarrierâĂŞAssisted Intrinsic Photoresponse in Graphene. *Science* **2011**, *334*, 648−652.
(43) Koppens, F. H. L.; Mueller, T.; Avouris, P.; Ferrari, A. C.; Vitiello, M.; Polini, M. Photodetectors based on graphene, other two-dimensional materials and hybrid systems. *Nat. Nanotechnol.* **2014**, *9*, 780−793.
(44) Freitag, M.; Chiu, H. Y.; Steiner, M.; Perebeinos, V.; Avouris, P. Thermal infrared emission from biased graphene. *Nat. Nanotechnol.* **2010**, *5*, 497−501.
(45) Kim, Y. D.; Kim, H.; Cho, Y.; Ryoo, J. H.; Park, C.-H.; Kim, P.; Kim, Y. S.; Lee, S.; Li, Y.; et al. Bright visible light emission from graphene. *Nat. Nanotechnol.* **2015**, *10*, 676−681.
(46) Lui, C. H.; Mak, K. F.; Shan, J.; Heinz, T. F. Ultrafast Photoluminescence from Graphene. *Phys. Rev. Lett.* **2010**, *105*, 127404−4.
(47) Chen, C. F.; Park, C. H.; Boudouris, B. W.; Horng, J.; Geng, B.; Girit, C.; Zettl, A.; Crommie, M. F.; Segalman, R. A.; Louie, S. G.; Wang, F. Controlling inelastic light scattering quantum pathways in graphene. *Nature* **2011**, *471*, 617−620.
(48) Stoehr, R. J.; Kolesov, R.; Pflaum, J.; Wrachtrup, J. Fluorescence of laser-created electron-hole plasma in graphene. *Phys. Rev. B: Condens. Matter Mater. Phys.* **2010**, *82*, No. 121408R-4.
(49) Liu, W.-T.; Wu, W.; Schuck, P. J.; Salmeron, M.; Shen, Y. R.; Wang, F. Nonlinear broadband photoluminescence of graphene induced by femtosecond laser irradiation. *Phys. Rev. B: Condens. Matter Mater. Phys.* **2010**, *82*, No. 081408R-4.
(50) Sun, Z.; Hasan, T.; Torrisi, F.; Popa, D.; Privitera, G.; Wang, F.; Bonaccorso, F.; Basko, D. M.; Ferrari, A. C. Graphene Mode-Locked Ultrafast Laser. *ACS Nano* **2010**, *4*, 803−810.
(51) Mics, Z.; Tielrooij, K. J.; Parvez, K.; Jensen, S. A.; Ivanov, I.; Feng, X.; Müllen, K.; Bonn, M.; Turchinovich, D. Ultrafast nonlinear optical response of Dirac fermions in graphene. *Nat. Commun.* **2015**, *6*, 7655.

DOI: 10.1021/acsphotonics.9b00928
ACS Photonics 2019, 6, 2841−2849

(52) Hafez, H. A.; Kovalev, S.; Deinert, J.-C.; Mics, Z.; Green, B.; Awari, N.; Chen, M.; Germanskiy, S.; Lehnert, U.; Teichert, J.; Wang, Z.; et al. Extremely efficient terahertz high-harmonic generation in graphene by hot Dirac fermions. *Nature* **2018**, *561*, 507−511.
(53) Soavi, G.; Wang, G.; Rostami, H.; Purdie, D. G.; De Fazio, D.; Ma, T.; Luo, B.; Wang, J.; Ott, A. K.; Yoon, D.; et al. Broadband, electrically tunable third-harmonic generation in graphene. *Nat. Nanotechnol.* **2018**, *13*, 583−588.
(54) Jiang, T.; Huang, D.; Cheng, J.; Fan, X.; Zhang, Z.; Shan, Y.; Yi, Y.; Dai, Y.; Shi, L.; Liu, K.; et al. Gate-tunable third-order nonlinear optical response of massless Dirac fermions in graphene. *Nat. Photonics* **2018**, *12*, 430−436.
(55) Alexander, K.; Savostianova, N. A.; Mikhailov, S. A.; Kuyken, B.; Van Thourhout, D. Electrically Tunable Optical Nonlinearities in Graphene-Covered SiN Waveguides Characterized by Four-Wave Mixing. *ACS Photonics* **2017**, *4*, 3039−3044.
(56) Squier, J. A.; Müller, M.; Brakenhoff, G. J.; Wilson, K. R. Third harmonic generation microscopy. *Opt. Express* **1998**, *3*, 315−324.
(57) Sun, C. H.; Chu, S.-W.; Tai, S.-P. Scanning second-harmonic/third-harmonic generation microscopy of gallium nitride. *Appl. Phys. Lett.* **2000**, *77*, 2331−2333.
(58) New, G. H. C.; Ward, J. F. Optical Third-Harmonic Generation in Gases. *Phys. Rev. Lett.* **1967**, *19*, 556−559.
(59) Lippitz, M.; van Dijk, M. A.; Orrit, M. Third-Harmonic Generation from Single Gold Nanoparticles. *Nano Lett.* **2005**, *5*, 799−802.
(60) Grinblat, G.; Li, Y.; Nielsen, M. P.; Oulton, R. F.; Maier, S. A. Enhanced Third Harmonic Generation in Single Germanium Nanodisks Excited at the Anapole Mode. *Nano Lett.* **2016**, *16*, 4635−4640.
(61) Shibanuma, T.; Grinblat, G.; Albella, P.; Maier, S. A. Efficient Third Harmonic Generation from MetalâĂŞDielectric Hybrid Nanoantennas. *Nano Lett.* **2017**, *17*, 2647−2651.
(62) Wang, R.; Chien, H. C.; Kumar, J.; Kumar, N.; Chiu, H.-Y.; Zhao, H. Third-Harmonic Generation in Ultrathin Films of MoS_2. *ACS Appl. Mater. Interfaces* **2014**, *6*, 314−318.
(63) Hong, S. Y.; Dadap, J. I.; Petrone, N.; Yeh, P. C.; Hone, J.; Osgood, R. M. Optical Third-Harmonic Generation in Graphene. *Phys. Rev. X* **2013**, *3*, 021014−10.
(64) Woodward, R. I.; Murray, R. T.; Phelan, C. F.; de Oliveira, R. E. P.; Runcorn, T. H.; Kelleher, E. J. R.; Li, S.; de Oliveira, E. C.; Fechine, G. J. M.; Eda, G. Characterization of the second- and third-order nonlinear optical susceptibilities of monolayer MoS_2 using multiphoton microscopy. *2D Mater.* **2017**, *4*, 011006−7.
(65) Hendry, E.; Hale, P. J.; Moger, J.; Savchenko, A. K.; Mikhailov, S. A. Coherent Nonlinear Optical Response of Graphene. *Phys. Rev. Lett.* **2010**, *105*, 097401−4.
(66) Li, X.; Cai, W.; An, J.; Kim, S.; Nah, J.; Yang, D.; Piner, R.; Velamakanni, A.; Jung, I.; Tutuc, E. Large-area synthesis of high-quality and uniform graphene films on copper foils. *Science* **2009**, *324*, 1312−1314.
(67) Bonaccorso, F.; Lombardo, A.; Hasan, T.; Sun, Z.; Colombo, L.; Ferrari, A. C. Production and processing of graphene and 2d crystals. *Mater. Today* **2012**, *15*, 564−589.
(68) Ferrari, A. C.; Meyer, J. C.; Scardaci, V.; Casiraghi, C.; Lazzeri, M.; Mauri, F.; Piscanec, S.; Jiang, D.; Novoselov, K. S.; Geim, A. K. Raman Spectrum of Graphene and Graphene Layers. *Phys. Rev. Lett.* **2006**, *97*, 187401−4.
(69) Das, A.; Pisana, S.; Chakraborty, B.; Piscanec, S.; Saha, S. K.; Waghmare, U. V.; Novoselov, K. S.; Krishnamurthy, H. R.; Geim, A. K.; Ferrari, A. C.; et al. Monitoring dopants by Raman scattering in an electrochemically top-gated graphene transistor. *Nat. Nanotechnol.* **2008**, *3*, 210−215.
(70) Basko, D. M.; Piscanec, S.; Ferrari, A. C. Electron-electron interactions and doping dependence of the two-phonon Raman intensity in graphene. *Phys. Rev. B: Condens. Matter Mater. Phys.* **2009**, *80*, 165413−10.
(71) Mak, K. F.; Ju, L.; Wang, F.; Heinz, T. F. Optical spectroscopy of graphene. *Solid State Commun.* **2012**, *152*, 1341−1349.
(72) Symphony II 1024 × 256 cryogenic open-electrode CCD detector quantum efficiency and grating (300 gr/mm, blazed 600 nm 510 19 140) relative efficiency from www.horiba.com.
(73) https://www.sigmaaldrich.com.
(74) Grosso, G.; Parravicini, P. *Solid State Physics*; Academic Press: Oxford, UK, 2000.
(75) Breusing, M.; Kuehn, S.; Winzer, T.; Malić, E.; Milde, F.; Severin, N.; Rabe, J. P.; Ropers, C.; Knorr, A.; Elsaesser, T. Ultrafast nonequilibrium carrier dynamics in a single graphene layer. *Phys. Rev. B: Condens. Matter Mater. Phys.* **2011**, *83*, 153410−4.
(76) Kotov, V. N.; Uchoa, B.; Pereira, V. M.; Guinea, F.; Castro Neto, A. H. Electron-Electron Interactions in Graphene: Current Status and Perspectives. *Rev. Mod. Phys.* **2012**, *84*, 1067−1125.
(77) Ku, H. H. J. Notes on the use of propagation of error formulas. *J. Res. Natl. Bur. Stand., Sect. C* **1966**, *70*, 263−273.
(78) Giuliani, G. F.; Vignale, G. *Quantum Theory of the Electron Liquid*; Cambridge University Press: Cambridge, UK, 2005.

DOI: 10.1021/acsphotonics.9b00928
ACS Photonics 2019, 6, 2841−2849